

The Clustering of High Redshift Galaxies in the Cold Dark Matter Scenario

Neal Katz^{1,4}, Lars Hernquist^{2,5}, and David H. Weinberg^{3,6}

ABSTRACT

We investigate the clustering of high redshift galaxies in five variants of the cold dark matter (CDM) scenario, using hydrodynamic cosmological simulations that resolve the formation of systems with circular velocities $v_c \geq 100 \text{ km s}^{-1}$ ($\Omega = 1$) or $v_c \geq 70 \text{ km s}^{-1}$ ($\Omega = 0.4$). Although the five models differ in their cosmological parameters and in the shapes and amplitudes of their mass power spectra, they predict remarkably similar galaxy clustering at $z = 2, 3$, and 4 . The galaxy correlation functions show almost no evolution over this redshift range, even though the mass correlation functions grow steadily in time. Despite the fairly low circular velocity threshold of the simulations, the high redshift galaxies are usually highly biased tracers of the underlying mass distribution; the bias factor evolves with redshift and varies from model to model. Predicted correlation lengths for the resolved galaxy population are $2 - 3 h^{-1} \text{ Mpc}$ (comoving) at $z = 3$. More massive galaxies tend to be more strongly clustered. These CDM models have no difficulty in explaining the strong observed clustering of Lyman-break galaxies, and some may even predict excessive clustering. Because the effects of bias obscure differences in mass clustering, it appears that Lyman-break galaxy clustering will not be a good test of cosmological models but will instead provide a tool for constraining the physics of galaxy formation.

Subject headings: Galaxies: formation, large scale structure of Universe

1. Introduction

Over the last three years, the combination of color selection from deep imaging surveys with spectroscopy from large aperture telescopes has revealed an abundant population of

¹ Department of Physics and Astronomy, University of Massachusetts, Amherst, MA, 01003

² Lick Observatory, University of California, Santa Cruz, CA 95064

³ Department of Astronomy, The Ohio State University, Columbus, OH 43210

⁴ nsk@kaka.phast.umass.edu

⁵ lars@helios.ucolick.org

⁶ dhw@astronomy.ohio-state.edu

star-forming galaxies in the high redshift universe (Steidel et al. 1996; Lowenthal et al. 1997). The remarkably rapid growth in surveys of these “Lyman-break” galaxies has created an essentially new observational field: the study of galaxy clustering at $z > 2$. The first step on this path was the discovery by Steidel et al. (1998a; hereafter SADGPK) of a sharp spike in the redshift distribution of Lyman-break galaxies in a $9' \times 18'$ field, implying that this galaxy population was already quite strongly clustered at $z = 3$. More recently Giavalisco et al. (1998a) have used the angular correlation function and the estimated redshift distribution of a Lyman-break galaxy sample to infer the spatial correlation function, obtaining a correlation length $r_0 = 2.1 \pm 0.5 h^{-1} \text{Mpc}$ (comoving, for $\Omega = 1$; $h \equiv H_0/100 \text{ km s}^{-1} \text{Mpc}^{-1}$). Adelberger et al. (1998, hereafter ASGDPK) have studied the variance of cell counts in a redshift survey of six $9' \times 9'$ fields and estimate a somewhat larger correlation length, $r_0 = 4.0 \pm 1.0 h^{-1} \text{Mpc}$ (again for $\Omega = 1$). Other attempts to measure the galaxy correlation function at high redshift include studies of angular clustering in the Hubble Deep Field (Villumsen, Freudling & da Costa 1997; Miralles & Pelló 1998) and analyses of 3-dimensional clustering of CIV absorption features in quasar spectra (Quashnock, Vanden Berk & York 1996; Quashnock & Vanden Berk 1997).

Rapid observational progress begets theoretical interpretations, and there have been numerous papers offering predictions of Lyman-break galaxy clustering in different cosmological models. Nearly all of these papers in practice calculate the clustering of dark matter halos, using either N-body simulations or the approximate analytic methods developed by Mo & White (1996) and Kaiser (1984). The N-body calculations (Bagla 1998ab; Jing 1998; Jing & Suto 1998; Wechsler et al. 1998) and analytic studies (Mo & Fukugita 1996; ASGDPK; Coles et al. 1998; Moscardini et al. 1998; SADGPK) agree on an essential qualitative conclusion: if the Lyman-break galaxies in current samples trace the massive tail of the halo population at $z \sim 3$, then they are expected to be highly biased tracers of the underlying mass distribution, as implied by the observed clustering strength. For this reason, models based on inflation and CDM can account reasonably well for the present clustering data with a variety of choices of cosmological parameters. ASGDPK turn this argument around to conclude that the most luminous Lyman-break galaxies must reside in massive halos because if they were low mass systems in more common halos — boosted to high rest-frame UV luminosity by bursts of star formation — then they would not exhibit the observed strong clustering.

All of these interpretations rest on the assumption that one can, at least for purposes of clustering calculations, make a one-to-one identification between the population of Lyman-break galaxies and the population of dark matter halos at $z \sim 3$. The analogous assumption at $z = 0$ is known to be incorrect: typical virialized halos today represent the common envelopes of galaxy groups or clusters, and predictions of the galaxy correlation function from CDM N-body simulations are sensitive to the way one chooses to populate these halos with galaxies (Gelb & Bertschinger 1994b). The one-to-one assumption may seem more plausible at $z \sim 3$ when the individual high mass halos have masses that are typical of individual galaxy halos today, but the galaxies themselves may be smaller at high redshift, and one might equally well imagine that the

relation between massive halos and galaxy groups is a scaled down version of the one that exists at $z = 0$. In a hydrodynamic simulation study of the population of damped Ly α absorbers, Gardner et al. (1997, figure 1) explicitly demonstrate that many dark halos identified at $z = 3$ with density contrast $\rho/\bar{\rho} \sim 200$ contain more than one galaxy.

Governato et al. (1998) have taken a somewhat different approach to predict the clustering of Lyman-break galaxies. They use a high resolution N-body simulation to model the formation and clustering of halos, but they use the semi-analytic galaxy formation prescriptions of Cole et al. (1994) and Baugh et al. (1998) to populate these halos with galaxies (a similar approach has been taken by Kauffmann et al. 1998). This technique substitutes an approximate description of gas cooling, star formation, and galaxy merging for the one-halo-one-galaxy assumption. In principle, this approach could yield significantly different clustering predictions, although the qualitative conclusion of Governato et al. (1998) — that the presently detected population of Lyman-break galaxies should be a highly biased tracer of structure — is similar to that of the papers cited earlier (and we will reach essentially the same conclusion here).

In this paper, we extend our earlier studies of galaxy clustering in hydrodynamic cosmological simulations (Katz, Hernquist & Weinberg 1992; Katz, Weinberg & Hernquist 1996, hereafter KWH) to an investigation of high redshift galaxy clustering in five variants of the CDM scenario (Peebles 1982; Blumenthal et al. 1984). Two of the simulations (the SCDM and CCDM models described below) are the ones analyzed in KWH and Weinberg, Hernquist, & Katz (1997, hereafter WHK), but we did not present galaxy correlation functions in those papers because even that short time ago it seemed that the clustering of $z = 3$ galaxies would not be accessible to observation for many years. The advantage of full hydrodynamic simulations over the semi-analytic galaxy formation method is that the crucial processes of dissipation and merging are treated much more realistically, without the idealizing approximations of spherical symmetry, isothermal profiles, and parameterized merging rates. Galaxy identification is straightforward and robust in high resolution hydrodynamic simulations because the dissipated objects stand out distinctly from the background and from each other, with overdensities of $10^3 - 10^6$ or even higher. The physics of galactic scale star formation and feedback is an uncertainty in both the semi-analytic and the hydrodynamic simulation approaches, but at least within the range of assumptions explored by KWH the inferred galaxy population is insensitive to details of the star formation prescription. Indeed, one finds nearly identical galaxy populations in simulations that include star formation and feedback and in simulations that have no star formation and identify galaxies directly as clumps of cold, dense gas (WHK, figure 10; Pearce 1998). The galaxy population is also completely insensitive to the presence of a photoionizing background in the mass range that we are presently able to resolve (WHK).

Since the observed-frame optical (rest-frame UV) luminosity of a $z = 3$ galaxy depends mainly on its instantaneous star formation rate, the identification of which of our simulated galaxies would make it into an observed Lyman-break galaxy sample *is* sensitive to our handling of star formation. Through most of this paper, we will make the simplifying assumption that a simulated

galaxy’s UV luminosity is a monotonically increasing function of its baryonic mass, but in §4 we will briefly discuss the possibility that episodic star formation introduces large scatter into this relationship. We will address issues related to the luminosity function of Lyman-break galaxies and the cosmic star formation history in a separate paper (for preliminary results see Weinberg, Katz, & Hernquist 1998, hereafter WKH).

The disadvantage of the numerical hydrodynamic approach to this problem is that computational expense forces us to adopt relatively small simulation volumes; in the case of the models described here, periodic cubes $11.111h^{-1}$ comoving Mpc on a side. This small volume affects our results in several ways. First, our simulation volume would contain only a handful of objects at the space density of the SADGPK sample, so we will mainly examine the clustering properties of the more numerous galaxies fainter than the magnitude limits of existing *spectroscopic* samples of high- z objects. Second, we have only a single realization of each model, and there might be significant statistical fluctuations in the clustering from one such volume to another. Third, the absence of waves larger than our box causes us to systematically underestimate the true amplitude of clustering. While the nonlinear scale of the dark matter is generally much smaller than the box at $z \geq 2$, the galaxies exhibit stronger clustering than the dark matter. Extreme regions like a proto-Coma cluster or a proto-Boötes void would be as large as our simulation volume (and the structure discovered by SADGPK might be roughly such a proto-Coma region). Our approach to estimating these finite volume effects (in §3.4 below) will be to assume that our hydrodynamic simulations correctly compute the *relative* amplitudes of the galaxy and dark matter correlation functions, allowing us to calibrate these bias factors in the hydrodynamic simulations and apply them to larger volume, lower resolution N-body simulations in order to estimate corrected correlation lengths. Our treatment still leaves us with statistical and systematic uncertainties in the clustering predictions, which are probably comparable in magnitude to the statistical and systematic uncertainties in the current measurements. We can hope for significant progress on both the theoretical and observational fronts over the next few years.

2. Methods and Models

We perform our simulations using TreeSPH (Hernquist & Katz 1989), a code that unites smoothed particle hydrodynamics (SPH; Lucy 1977; Gingold & Monaghan 1977) with the hierarchical tree method for computing gravitational forces (Barnes & Hut 1986; Hernquist 1987). Dark matter, stars, and gas are all represented by particles; collisionless material is influenced only by gravity, while gas is subject to gravitational forces, pressure gradients, and shocks. We include the effects of radiative cooling, assuming primordial abundances, and Compton cooling. Ionization and heat input from a UV radiation background are incorporated, assuming optically thin gas, using the radiation field computed by Haardt & Madau (1996). We use a simple prescription to turn cold, dense gas into collisionless “star” particles. The technique and its computational implementation are described in detail by KWH. In brief, gas becomes “eligible” to form stars if it

has a physical density corresponding to $n_{\text{H}} > 0.1 \text{ cm}^{-3}$ and an overdensity $\rho/\bar{\rho} > 56.7$ (equivalent to that at the virial radius of an isothermal sphere). The gas must also reside in a convergent flow and be locally Jeans unstable, although the density criteria themselves are usually sufficient to ensure this. Eligible gas is converted to stars at a rate $d\ln\rho_g/dt = -c_*/t_g$, where t_g is the maximum of the dynamical time and the cooling time. We use $c_* = 0.1$ for the simulations here, but KWH show that the simulated galaxy population is insensitive to an order-of-magnitude change in c_* , basically because the star formation rate is forced into approximate balance with the rate at which gas cools and condenses out of the hot halo. When star formation occurs, supernova heating is added to the surrounding gas assuming a standard IMF from 0.1 to $100M_{\odot}$ and that stars above $8M_{\odot}$ become supernovae. Each supernova adds 10^{51} ergs of thermal energy to the system.

Because it uses a Lagrangian hydrodynamics algorithm and individual particle time steps, TreeSPH makes possible simulations with the enormous dynamic range needed to study galaxy formation in a cosmological context. In SPH, gas properties are computed by averaging or “smoothing” over a fixed number of neighboring particles, 32 in the calculations here. When matter is distributed homogeneously, all particles have similar smoothing volumes. However, smoothing lengths in TreeSPH are allowed to decrease in collapsing regions, in proportion to the interparticle separation, thus increasing the spatial resolution in precisely those regions where a high dynamic range is needed. In underdense regions, the smoothing lengths are larger, but this is physically reasonable because the gas distribution *is* smoother in these regions, requiring fewer particles for an accurate representation. TreeSPH allows particles to have individual time steps according to their physical state, so that the pace of the overall computation is not driven by the small fraction of particles requiring the smallest time steps. In the calculations described here, the largest allowed timestep is 3.25×10^6 years. The smallest allowed timestep is 16 times smaller, or 2.03×10^5 years. If the Courant condition would demand a timestep smaller than this minimum, we degrade the gas resolution (increase the SPH smoothing length) so that the Courant condition is satisfied. The timestep criteria are detailed further in KWH and Quinn et al. (1998); we set the tolerance parameter $\epsilon_{\text{tol}} = 0.4$.

Here we present the results of five simulations, one each of five different cosmological models. All these simulations, of periodic cubes that are $11.111 h^{-1}\text{Mpc}$ on a side, use 2×64^3 particles and are evolved to $z = 2$. Each has a nominal gas mass resolution (32 gas particles) of $4.7 \times 10^9 (\Omega_b/0.05) M_{\odot}$ and a spatial resolution (gravitational softening length, in physical units) of $3(1+z)^{-1} h^{-1}\text{kpc}$ (equivalent Plummer softening). We adopt Walker et al.’s (1991) estimate of the baryon density, $\Omega_b = 0.0125h^{-2}$. We would not expect a higher value of Ω_b (*e.g.* Burles & Tytler 1997, 1998; Rauch et al. 1997) to alter our clustering results, but it would increase the baryonic mass (and presumably the luminosity) of galaxies at fixed space density. We adopt the same Fourier phases for the initial conditions of each model to minimize the impact of statistical fluctuations in our finite simulation volume on the comparison between models.

Our first model is “standard” CDM (SCDM), with $\Omega = 1$, $h = 0.5$. The power spectrum

is normalized so that the rms amplitude of mass fluctuations in $8 h^{-1}\text{Mpc}$ spheres, linearly extrapolated to $z = 0$, is $\sigma_8 = 0.7$. This normalization is consistent with (but somewhat higher than) that advocated by White, Efstathiou & Frenk (1993) to match the observed masses of rich galaxy clusters. However, it is inconsistent with the normalization implied by the COBE-DMR experiment. Our second model (CCDM) is identical to the first one except that $\sigma_8 = 1.2$, consistent with the 4-year COBE data (Bennett et al. 1996) but inconsistent with the $z = 0$ cluster population. The third model, OCDM, assumes an open universe with $\Omega = 0.4$, $h = 0.65$, and $\sigma_8 = 0.75$. It is COBE-normalized (Ratra et al. 1997) and produces an acceptable cluster mass function (Cole et al. 1997). The fourth model, a nonzero- Λ CDM model (LCDM), has $\Omega = 0.4$, $\Lambda = 0.6$, $h = 0.65$, and an inflationary fluctuation spectrum tilted ($n = 0.93$) so that it simultaneously matches the COBE and cluster constraints. The fifth model (TCDM) is an $\Omega = 1$, $h = 0.5$ model that also has a tilted inflationary spectrum ($n = 0.8$) chosen so that it matches COBE and cluster constraints. We list the parameters of all the models in Table 1. We also include a lower resolution simulation of the SCDM model evolved to $z = 0$ (from KWH). This simulation has 1/2 the spatial resolution and 1/8th the mass resolution of the other simulations, and it does not incorporate a photoionizing background.

As we discuss below, the interplay between the dynamics of the gas and the microphysical processes that influence its thermal state leads to the development of a three phase medium. In what follows we are particularly interested in the cold, dense component, which we identify with forming galaxies. These clumps of gas are at sufficiently high overdensity that stars form readily in them. Because the knots of cold gas particles and star particles are compact and distinct, it is easy to group them into simulated “galaxies.” The specific algorithm that we adopt is SKID (Spline Kernel Interpolative DENMAX; KWH, <http://www-hpcc.astro.washington.edu/tools/SKID/>), which identifies galaxies as gravitationally bound groups of cold gas and star particles that are associated with a common density maximum. The approach is inspired by Gelb & Bertschinger’s (1994a) DENMAX algorithm, but instead of defining gradients of the density field on an Eulerian mesh, it uses the SPH smoothing kernel to calculate Lagrangian density gradients. Only star particles and gas particles that have $\rho/\bar{\rho} \geq 1000$ and $T \leq 30,000$ K are eligible to be galaxy particles. We require a SKID group to contain at least eight particles in order to count it as a galaxy. While eight may seem a dangerously low number, the 32-particle averaging in SPH ensures that any collection of eight cold, high density particles must reside in a significantly more massive

Table 1: Models

Model	Ω	Λ	H_0	Ω_b	σ_8	n
SCDM	1.0	0.0	50	0.05	0.7	1.0
CCDM	1.0	0.0	50	0.05	1.2	1.0
OCDM	0.4	0.0	65	0.03	0.75	1.0
LCDM	0.4	0.6	65	0.03	0.8	0.93
TCDM	1.0	0.0	50	0.05	0.54	0.80

overdense background.

It is useful to express the resolution limit of the simulations in terms of the minimum circular velocity of halos in which we can resolve galaxies. Gardner et al. (1997) examined all halos in our SCDM simulation and found that only those with $v_c \geq 100 \text{ km s}^{-1}$ (measured at the virial radius) contained dense, cold objects corresponding to galaxies. We have applied the same analysis to our other models and find that the limit is $v_c \geq 100 \text{ km s}^{-1}$ in the $\Omega = 1$ models and $v_c \geq 70 \text{ km s}^{-1}$ in the low- Ω models (LCDM, OCDM). Although we cannot be certain that our results for galaxies above this mass limit do not suffer from finite resolution effects, the tests of Owen, Weinberg, & Villumsen (1998) for self-similar evolution in hydrodynamic simulations with scale-free initial conditions suggest that once a simulation has enough resolution to follow the formation of radiatively cooled gas clumps it obtains robust results for the subsequent growth and mergers of these objects.

3. Results

3.1. The High Redshift Galaxy Populations

As discussed in KWH and WKH, the evolution of the dark matter in the SPH simulations is similar to that in collisionless N-body simulations. The gas component, with a mass fraction that ranges from 0.050 to 0.074 in the different models, has little dynamical effect on the dark matter except in small regions surrounding the densest concentrations of cold gas. Gravitational instability produces a network of filaments and clumps containing both dark matter and gas, with the most prominent clumps residing at the intersections of filaments. When gas falls into a dark matter potential well, it is shock heated to roughly the virial temperature, converting its kinetic infall energy into thermal energy. The gas is supported against further collapse by thermal pressure. However, the densest gas is able to dissipate energy through atomic and Compton cooling processes, so it loses pressure support and settles into highly overdense knots within the dark halos. These clumps are so dense that they remain cold even when mergers occur or when they fall into larger halos. They are also much more resistant to tidal disruption than the relatively puffy dark matter halos that form in a purely dissipationless simulation, so the clumps can survive as distinct entities even when their parent halos merge.

At high redshift the gas in SPH simulations resides in three main components: low density, highly photoionized gas with $\rho/\bar{\rho} \lesssim 10$ and $T \lesssim 10^5 \text{ K}$, shock heated gas with typical overdensity $\rho/\bar{\rho} \sim 10\text{--}10^4$ and $T \sim 10^5\text{--}10^7 \text{ K}$, and radiatively cooled, dense gas with $\rho/\bar{\rho} \gtrsim 1000$ and $T \sim 10^4 \text{ K}$ (see KWH, figure 3). The first component gives rise to the Ly α forest, the second component is associated with hot gas halos of galaxies, galaxy groups, and clusters, and the third component is associated with damped Ly α systems and high redshift galaxies. In simulations with star formation, gas from this third component is converted steadily into stars.

Figure 1 shows the spatial distribution of galaxies at $z = 3$ for the five models, with the galaxies identified by the procedure described in §2. Each galaxy is represented by a circle whose area is proportional to its baryonic mass (cold gas plus stars). The concentration of galaxies in the middle right of the panels becomes a small cluster of galaxies by $z = 0$, at least in the SCDM model (KWH; WKH). For SCDM, CCDM, and TCDM the angular size of each comoving panel at $z = 3$ is 12.7 arc minutes, and the redshift depth is $\Delta z = 0.0297$. For OCDM, the angular size is 9.5 arc minutes with $\Delta z = 0.0220$, and for LCDM model the angular size is 9.3 arc minutes with $\Delta z = 0.0190$. The redshift depths of the simulation volumes are therefore small compared to the survey volume of SADGPK, who observed a field $17.64' \times 8.74'$ and found Lyman-break galaxies between $z = 2.7$ and $z = 3.4$, i.e., $\Delta z = 0.7$.

The more massive galaxies are predominantly stellar and the less massive ones are more gas-rich, though this trend could be partly an artifact of limited resolution, which influences small galaxies more than larger ones. By $z = 3$, the largest galaxies already have baryonic masses of $2.8 \times 10^{11} M_\odot$ in the CCDM model, but they have reached a baryonic mass of only $2.8 \times 10^{10} M_\odot$ in the TCDM model. This difference directly reflects the higher amplitude of mass fluctuations in the CCDM model; the remaining models have intermediate fluctuation amplitudes and intermediate galaxy masses.

The upper left panel of Figure 2 shows the dark matter particle distribution from a pure N-body simulation of the SCDM model, started from the same initial conditions as the SPH simulation and evolved with the same simulation code and numerical parameters. The dark matter distribution of the SPH simulation itself would be essentially indistinguishable at the level of detail visible on this plot. Figure 2b shows the SPH galaxy distribution, repeated from Figure 1. Comparing these two panels shows that the galaxy distribution traces the prominent features of the underlying mass distribution. However, randomly sampling the dark matter particles to the space density of the galaxies produces a distribution that is clearly less structured (Fig. 2c). This comparison demonstrates visually the point that we will quantify in the next section: the high-redshift galaxies in CDM models are highly biased tracers of the underlying structure, concentrated in clumps and filaments and avoiding underdense regions.

The remaining panels of Figure 2 show the populations of dark matter halos in the N-body simulation, identified by different algorithms. For Figure 2d we adopt the most widely used procedure for defining halos, the “friends-of-friends” (FOF) algorithm with linking parameter $d_l = 0.2$ in units of the mean interparticle separation (see, e.g., Frenk et al. 1988; the implementation used here is available at <http://www-hpcc.astro.washington.edu/tools/FOF/>). We select the 245 most massive FOF halos, so that the number of halos is equal to the number of SPH galaxies in the panel above. The mass scale for determining the sizes of symbols has been shifted by a factor $\Omega/\Omega_b = 20$. If each FOF halo contained a single galaxy with a baryon-to-dark-matter ratio equal to the universal value, Figures 2b and 2d would be identical. The bottom panels of Figure 2 show the halo populations identified by FOF with a shorter linking length, $d_l = 0.1$, corresponding to a higher effective threshold density, and by the SKID algorithm

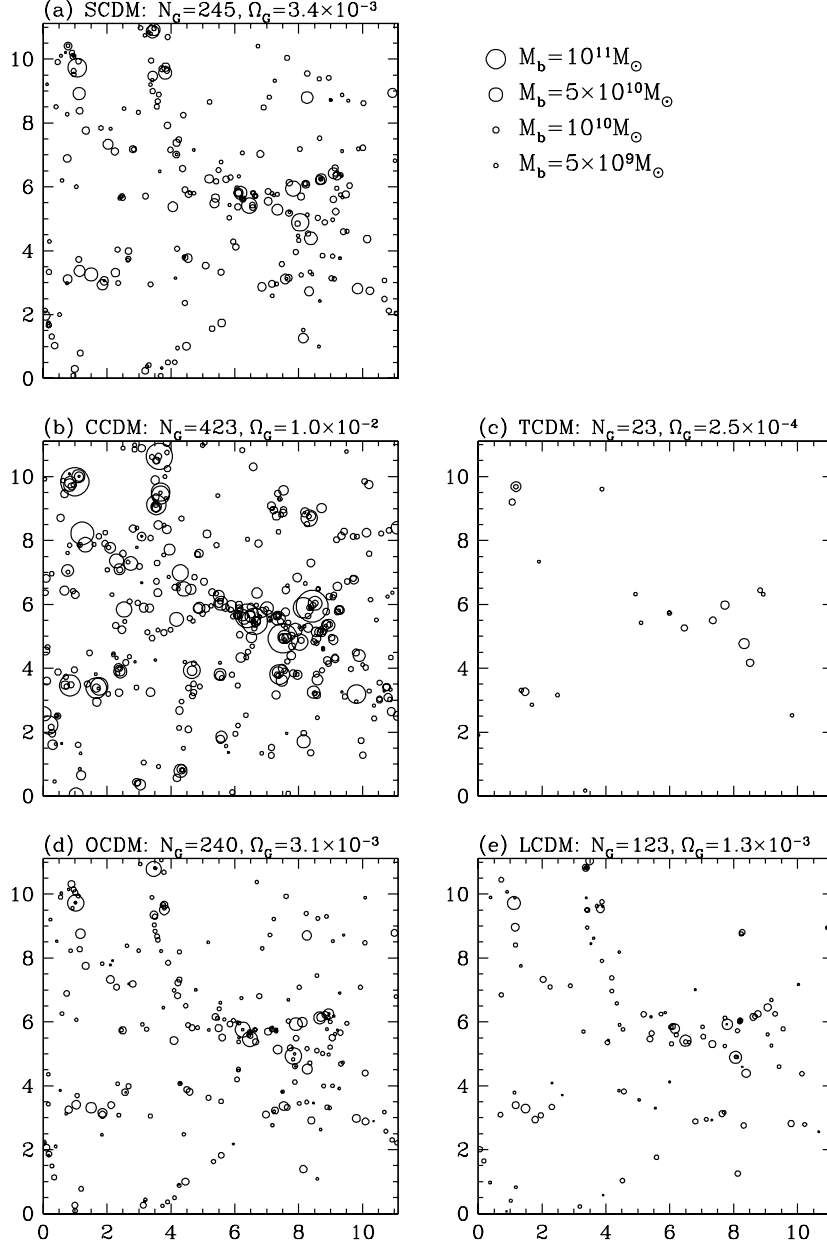


Fig. 1.— The distribution of “galaxies” in each of the models at $z = 3$. Each galaxy is represented by a circle whose area is proportional to its baryonic mass (cold gas plus stars). The total number of galaxies and Ω_g , the fraction of the critical density in galactic baryonic mass, is also indicated for each model. The axes are marked in comoving h^{-1} Mpc.

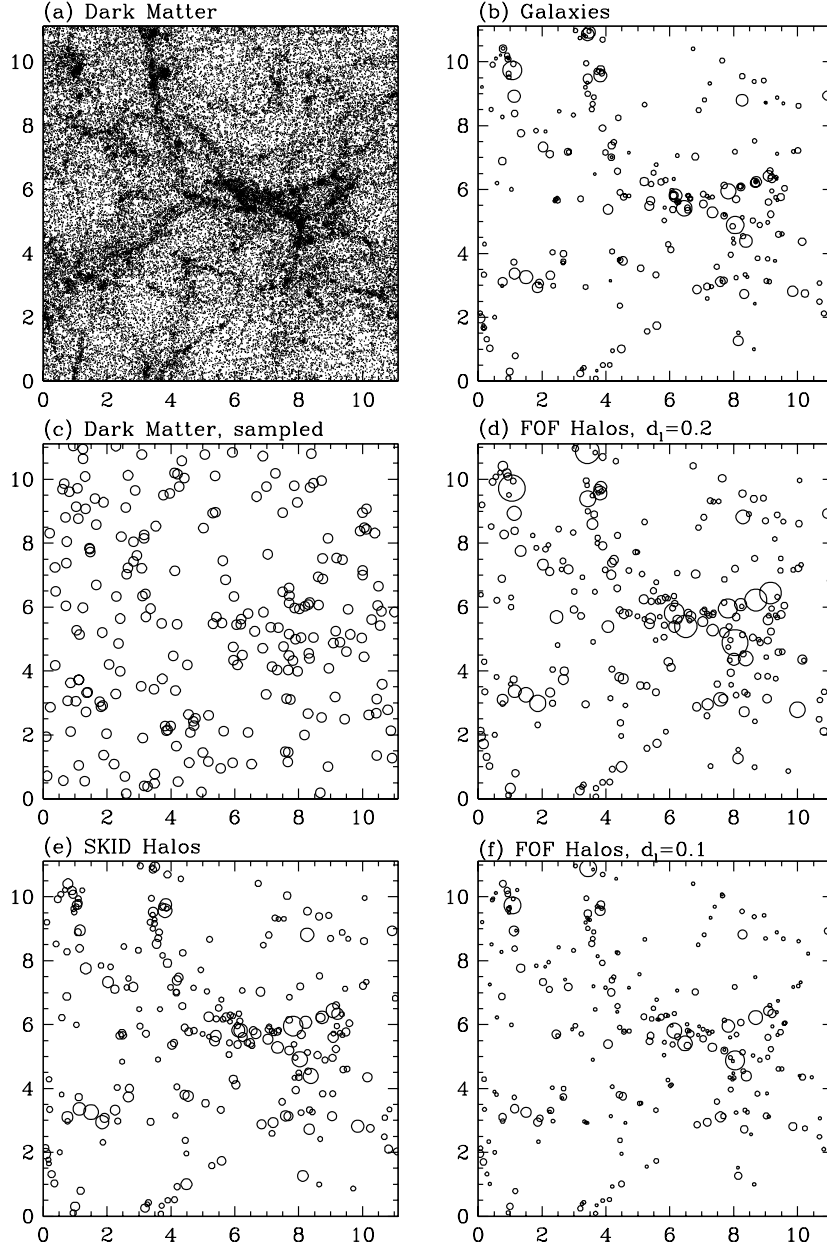


Fig. 2.— Distributions of dark matter, galaxies, and halos in the SCDM model at $z = 3$. (a) Dark matter particles (randomly selected subset of 1 in 4) from a purely gravitational, N-body simulation. (b) SPH galaxies, repeated from Fig. 1a. (c) Random subset of 245 dark matter particles from (a), equal to the number of SPH galaxies in (b). (d) The 245 most massive halos from the N-body simulation, identified by the friends-of-friends (FOF) algorithm with linking parameter $d_l = 0.2$. (e) Same as (d) for SKID halos. (f) Same as (d) for linking parameter $d_l = 0.1$.

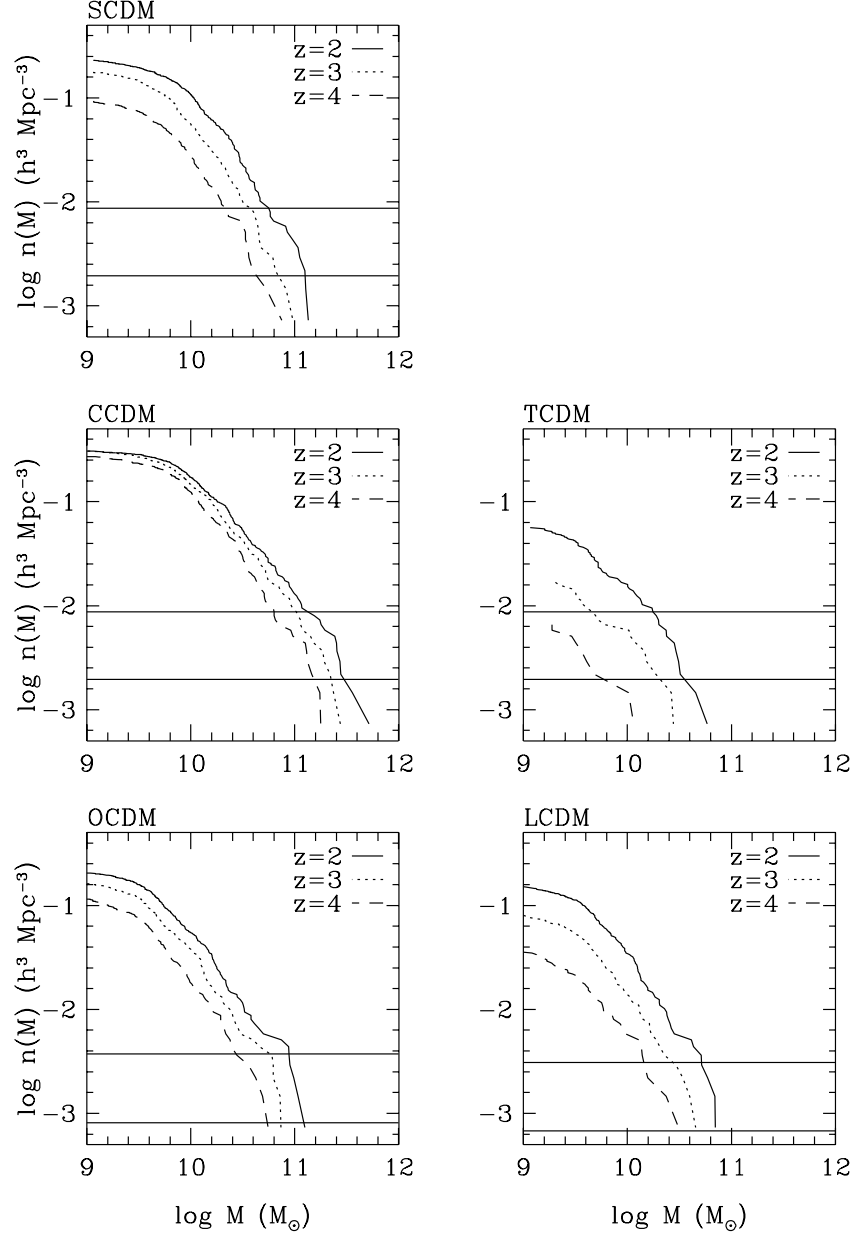


Fig. 3.— Cumulative baryonic mass function in the different models at the indicated redshifts: $n(M)$ is the comoving number density of galaxies whose baryonic mass exceeds M . The solid horizontal lines mark the space density of Lyman-break galaxies in the SADGPK sample (lower line) and the Lowenthal et al. (1997) sample (upper line).

(with a smoothing scale of 64 particles and an overdensity threshold of 50).

Figure 2 shows that the dark matter halos are also biased tracers of structure at $z = 3$ — their space distribution resembles the galaxy distribution much more than it resembles the dark matter distribution. However, while the halo and galaxy distributions give a similar overall picture, there is clearly not a one-to-one match between halos and galaxies in the high density regions that dominate statistical clustering measures, and the halo population itself depends on the specific identification algorithm. It is these differences between halos and galaxies and among halo identification algorithms themselves that motivates the use of hydrodynamic simulations to study high-redshift galaxy clustering. As already noted, the galaxy population in high resolution SPH simulations is insensitive to “microphysical” assumptions about star formation, feedback, and photoionization, at least within the range tested by KWH, WHK, and Pearce (1998). Furthermore, because dissipation produces highly overdense objects, there is essentially no ambiguity in grouping cold gas and star particles into galaxies: N-body halos overlap, but SPH galaxies do not. While halo-based models can provide a useful qualitative guide to expectations of high-redshift structure, collisionless N-body simulations do not include the dissipational physics needed to obtain robust and accurate quantitative predictions of galaxy clustering at any redshift. We must also acknowledge, however, that the small volume of our current SPH simulations is also a significant limitation, and that larger and more ambitious simulations will be needed to take advantage of improvements in observational constraints.

Figure 3 plots the cumulative baryonic mass function of the galaxies in the five models at $z = 2, 3$, and 4. The high end of the mass function shifts to the right in each of the models as more gas condenses into galaxies and small galaxies merge. In the highest amplitude model, CCDM, the low mass end ceases to evolve as smaller galaxies merge into larger ones and are not replaced. Limited mass resolution almost certainly causes the turnover in all models at the low mass end, and it is likely responsible for the lack of late evolution in the CCDM model at these masses.

As one might expect, given the relative power on galactic scales, the CCDM model has the most galaxies at $z = 2, 3$, and 4, followed by OCDM, SCDM, LCDM, TCDM. The cumulative mass function evolves fastest in the models with the weakest high-redshift mass fluctuations, LCDM and TCDM. The horizontal lines mark the space densities of systems detected in the Lyman-break surveys of SADGPK and Lowenthal et al. (1997). SADGPK survey a volume of $\sim 30,400 h^{-3}\text{Mpc}^3$ ($\sim 72,900 h^{-3}\text{Mpc}^3$; $88,000 h^{-3}\text{Mpc}^3$) for $\Omega = 1$ ($\Omega = 0.4$; $\Omega = 0.4$, $\Lambda = 0.6$) and obtain spectroscopic confirmation of 59 Lyman-break galaxies, implying a space density of $1.94 \times 10^{-3} h^3\text{Mpc}^{-3}$ ($8.10 \times 10^{-4} h^3\text{Mpc}^{-3}$; $6.70 \times 10^{-4} h^3\text{Mpc}^{-3}$). Lowenthal et al. (1997) observe to a fainter magnitude limit and find a number density of $8.8 \times 10^{-3} h^3\text{Mpc}^{-3}$ ($3.7 \times 10^{-3} h^3\text{Mpc}^{-3}$; $3.1 \times 10^{-3} h^3\text{Mpc}^{-3}$). On average, we would expect 2.7 (1.1; 0.9) galaxies at the SADGPK density and 12.1 (5.1; 4.3) galaxies at the Lowenthal et al. density in our simulation volume. The more extensive ASGDPK sample has a space density similar to that of SADGPK. If our CDM models are representative of the real universe, then the objects in existing spectroscopic samples of Lyman-break galaxies represent just the luminous tip of the full population of galaxies

at these redshifts, presumably corresponding to the largest few circles in the panels of Figure 1.

3.2. Galaxy Correlation Functions

Figure 4 presents the principal results of this paper, the galaxy correlation functions in our five cosmological models at $z = 2, 3$, and 4. We calculate the correlation function for all the galaxies in the simulation volume. As discussed in §2 above, the effective circular velocity limits of the simulations are $v_c \geq 100 \text{ km s}^{-1}$ in the SCDM, CCDM, and TCDM models and $v_c \geq 70 \text{ km s}^{-1}$ in the OCDM and LCDM models. We also calculate the correlation function at $z = 0$ for the SCDM model using the lower resolution simulation mentioned in §2, which has an effective circular velocity limit $v_c \geq 200 \text{ km s}^{-1}$. The TCDM results are noisy except at $z = 2$ because this model does not form many galaxies above our resolution limit at higher redshifts. Points show the galaxy correlation function at various redshifts and solid lines show the dark matter correlation functions, which increase monotonically in time as mass fluctuations grow. For comparison purposes, the dashed line in each panel shows a power law correlation function,

$$\xi(r) = (r/r_0)^\gamma, \quad (1)$$

with a slope $\gamma = -1.8$ and a correlation length $r_0 = 2.0 h^{-1}\text{Mpc}$ (comoving units are used throughout). In all cases with adequate statistics, the galaxy correlation function is well described by a power law over 2 decades in r (roughly four decades in ξ), though the slope is usually closer to -2.0 than to -1.8 .

Figure 4 exhibits several striking features. In all models, the galaxy correlation function shows little or no evolution between $z = 4$ and $z = 2$, although the dark matter correlation function grows steadily stronger over this period. The galaxy correlations are more pronounced than the dark matter correlations in virtually all cases, sometimes by a factor of 10 or more. This strong bias exists despite our fairly low circular velocity threshold and correspondingly high galaxy space density. Perhaps most remarkably, there is very little difference in the galaxy correlation function from one model to another, even though these models have different cosmological parameters and different mass fluctuation amplitudes. To the extent that there are differences between models, it is the model with the weakest mass fluctuations (TCDM) that has the strongest galaxy correlations at $z = 2$, and it is the model with the strongest mass correlations (CCDM) that has the weakest galaxy correlations. Within an individual model, there is often a slight drop in the galaxy correlation amplitude from $z = 4$ to $z = 2$.

The correlation function results quantify the visual impressions of Figures 1 and 2: the high redshift galaxies form in “special” locations that trace the skeleton of structure in the mass distribution. This skeleton is essentially the same from one model to another, even though its contrast in the mass distribution depends on the amplitude of mass fluctuations in the model. Between $z = 4$ and $z = 2$, an increasing amount of dark matter flows into this skeleton, but this does not substantially increase the amplitude of galaxy clustering because the galaxies are already

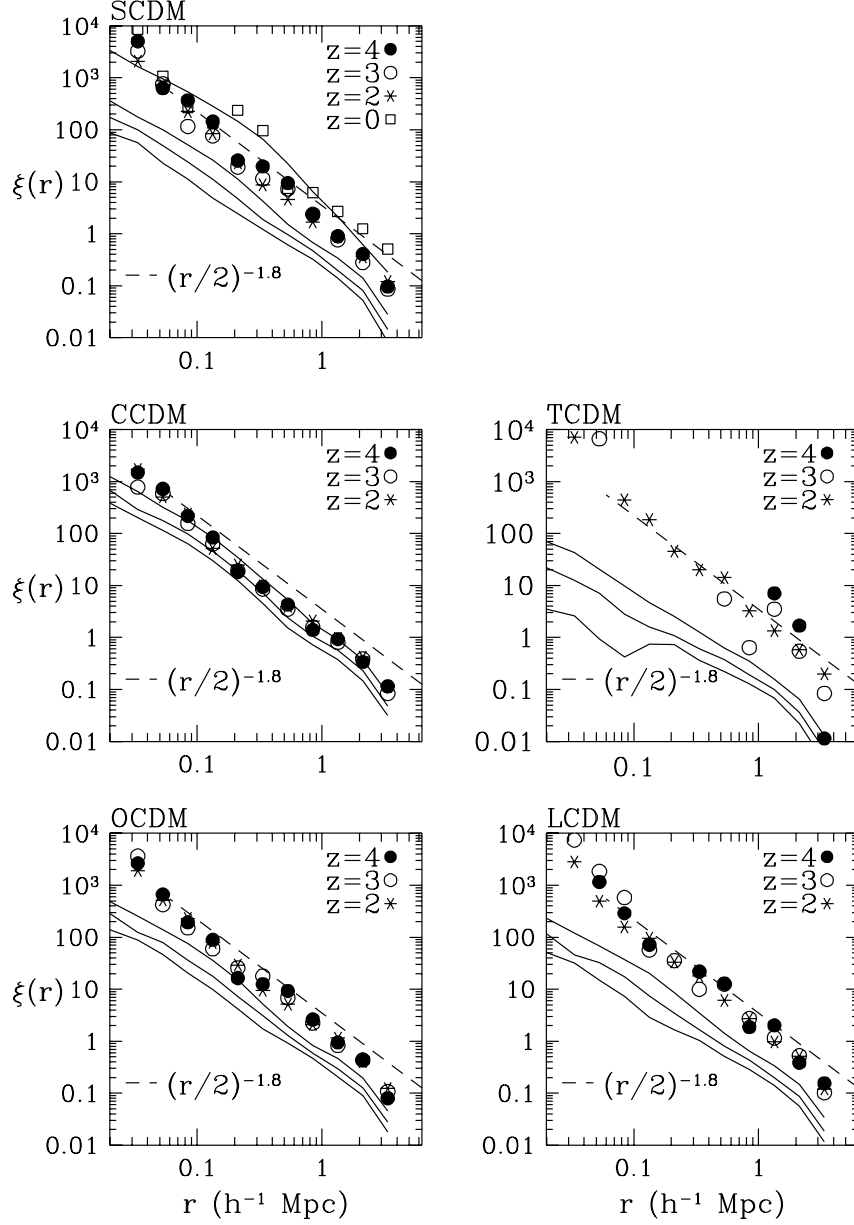


Fig. 4.— Galaxy correlation functions, in comoving distance units. Symbols show the correlation functions of SPH galaxies at the indicated redshifts. Solid lines show the dark matter correlation functions at the same redshifts (increasing in amplitude with decreasing redshift). The dashed line is a power law with a slope of -1.8 and a correlation length of $2.0 h^{-1}\text{Mpc}$.

there. Only at low redshifts does the gravitational clustering of the dark matter begin to carry the galaxies into higher contrast structures and increase their correlation function, as seen in the $z = 2$ to $z = 0$ evolution of the SCDM model.

Figure 5 compares the galaxy and mass correlation functions measured from the SCDM SPH simulation at $z = 3$ to correlation functions of FOF halos from the SCDM N-body simulation at the same redshift. For Figure 2a, we select the 245 most massive halos, so that the space density of the halos is equal to the space density of the SPH galaxies. The FOF halo identification method effectively precludes halos from being very close neighbors, so there are no pairs (implying $\xi = -1$) at $r < 0.2 h^{-1}\text{Mpc}$ for linking parameter $d_l = 0.2$. At larger separations the halo correlation function is slightly weaker than the galaxy correlation function, but it is substantially stronger than the dark matter correlation function, as one would expect based on Figure 2. Halos selected with $d_l = 0.1$ have a similar correlation function, except that $\xi(r)$ continues to rise in to smaller separations. In both cases, the halos are positively biased, despite the relatively high comoving space density of $0.18 h^3\text{Mpc}^{-3}$. Figure 5b compares the correlation function of the 30 most massive SPH galaxies to the 30 most massive FOF halos, with $\xi(r)$ averaged over larger bins to reduce noise. The clustering of the galaxies increases slightly with the higher mass threshold (a point we will return to later), but the clustering of the $d_l = 0.2$ halos increases more, so that at intermediate separations they are now more strongly clustered than the galaxies.

For nearly all cases in Figure 4, the galaxy correlation function is close to a power law in the range $0.04 h^{-1}\text{Mpc} < r < 4 h^{-1}\text{Mpc}$. Tables 2 and 3 list the parameters r_0 and γ , respectively, of power law fits to these correlation functions, where r_0 is the correlation length and γ the power law index (see equation [1]). We perform the fits in log space over the above radial range, using Poisson counting errors to estimate the error in $\xi(r)$ in each radial bin. At $z = 3$ the correlation lengths range from $r_0 = 1.13 h^{-1}\text{Mpc}$ to $r_0 = 1.64 h^{-1}\text{Mpc}$, and the power law slopes range from $\gamma = -1.97$ to $\gamma = -2.46$. Note, however, that our finite box size causes us to systematically underestimate r_0 and to systematically overestimate $|\gamma|$, a point that we will return to in §3.4 below. The uncertainties listed in Tables 2 and 3 are the formal uncertainties of the parameter fits, but they do not include the statistical uncertainty that arises because we have only a single realization of each model. We cannot assess the magnitude of this uncertainty until we perform more simulations. However, these are reasonable error bars to use when comparing one model to another, since we employ the same initial Fourier phases in each simulation.

Table 2: Correlation Lengths, r_0 , in $h^{-1}\text{Mpc}$

Model	$z = 4$	$z = 3$	$z = 2$	$z = 1$	$z = 0$
SCDM	1.29 ± 0.03	1.16 ± 0.02	1.20 ± 0.01	1.72 ± 0.10	2.35 ± 0.08
CCDM	1.17 ± 0.01	1.13 ± 0.01	1.23 ± 0.01	-	-
OCDM	1.28 ± 0.02	1.27 ± 0.02	1.28 ± 0.01	-	-
LCDM	1.51 ± 0.07	1.41 ± 0.03	1.35 ± 0.02	-	-
TCDM	2.04 ± 0.34	1.64 ± 0.15	1.59 ± 0.06	-	-

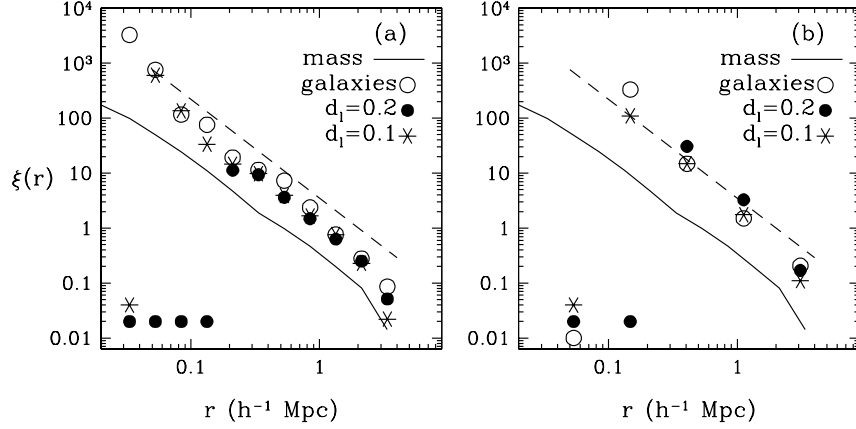


Fig. 5.— Correlation functions of dark matter (solid line), SPH galaxies (open circles), and FOF halos identified with linking parameter $d_l = 0.2$ (filled circles) and $d_l = 0.1$ (asterisks), for the SCDM model at $z = 3$. Bins at small separations containing no pairs are indicated by points near the horizontal axis. The dashed line shows a power law $\xi(r) = (r/2)^{-1.8}$. (a) Comparison of all (245) SPH galaxies to the most massive 245 halos. (b) Comparison of the 30 most massive SPH galaxies to the 30 most massive halos.

Table 3: Power law slope, γ , of the correlation functions

Model	$z = 4$	$z = 3$	$z = 2$	$z = 1$	$z = 0$
SCDM	-2.25 ± 0.04	-2.18 ± 0.03	-1.98 ± 0.02	-2.02 ± 0.09	-2.12 ± 0.05
CCDM	-1.98 ± 0.02	-1.97 ± 0.02	-1.97 ± 0.02	-	-
OCDM	-2.18 ± 0.04	-2.09 ± 0.03	-2.00 ± 0.02	-	-
LCDM	-2.21 ± 0.08	-2.28 ± 0.04	-2.06 ± 0.03	-	-
TCDM	-2.82 ± 0.19	-2.46 ± 0.14	-2.10 ± 0.07	-	-

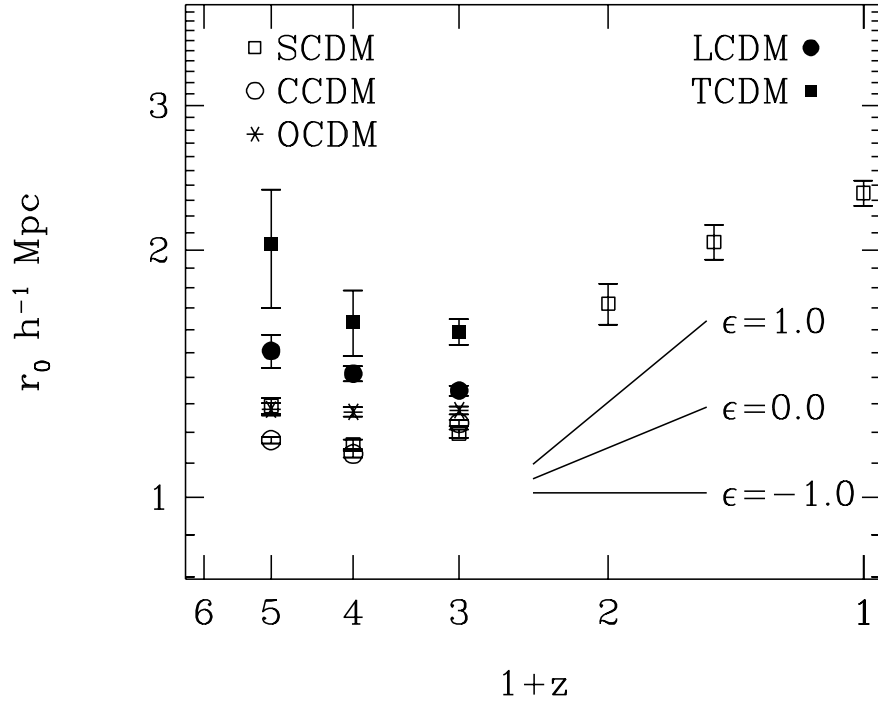


Fig. 6.— Redshift evolution of the galaxy correlation length. Solid lines show the expected growth rates for different values of ϵ (eq. [2]).

Figure 6 plots the redshift evolution of the correlation lengths r_0 . Within a given model, there is little change in r_0 from $z = 4$ to $z = 2$. To the extent that there is evolution over this redshift interval, r_0 declines slightly in the models with the weakest mass fluctuations, TCDM and LCDM, and stays flat or rises slightly in the models with stronger mass fluctuations, SCDM, OCDM, and CCDM. The SCDM points at $z = 1, 0.5$, and 0 are taken from the lower resolution simulation described in §2. At low redshift, the correlation length does increase with time, as gravitational clustering pulls galaxies and clusters into denser and larger structures.

In observational analyses and theoretical discussions, the evolution of the correlation function is often parameterized as a power law in redshift,

$$\xi(r, z) = (r/r_0)^\gamma (1+z)^{-(3+\epsilon+\gamma)} \quad (2)$$

where r_0 is the comoving correlation length (e.g., Groth & Peebles 1977; Efstathiou et al. 1991). This equation in turn implies

$$r_0(z) = r_0(1+z)^{1+(3+\epsilon)/\gamma}. \quad (3)$$

Two interesting, though not necessarily limiting, cases are a clustering pattern fixed in comoving coordinates, implying $\epsilon = -3 - \gamma$, and a clustering pattern that is dynamically bound and stable in physical coordinates, implying $\epsilon = 0$ (Groth & Peebles 1977; note that this is not the same as a fixed physical correlation length because the contrast of structure grows as the background density drops.) Linear fluctuation growth in an Einstein-de Sitter universe corresponds to $\epsilon = -1 - \gamma$.

The solid lines in Figure 6 show the r_0 evolution for $\epsilon = -1, 0$, and $+1$, corresponding to fixed comoving clustering, fixed physical clustering, and linear growth, respectively, for $\gamma = -2$. At high redshifts, r_0 is nearly fixed in comoving coordinates, with $\epsilon = -1$. For the SCDM model at lower redshift, we find evolution in between fixed physical clustering and linear growth. However, it is clear from Figure 6 that the power law parameterization of equation (2) can at best be an approximation over a rather narrow range of redshifts. Between $z = 4$ and $z = 0$, the predicted evolution of the galaxy correlation length is not described by a single power law, and in some cases it is not even monotonic.

3.3. Bias Factors

It is obvious from Figures 1 and 4 that the clustering of the SPH galaxies is biased relative to the clustering of the dark matter. In order to quantify this bias with a statistically robust measure, we define a bias factor $b(R)$ from the ratio of J_3 integrals:

$$b(R) = \left(\frac{J_{3,\text{gal}}(R)}{J_{3,\text{dark}}(R)} \right)^{0.5}, \quad \text{where} \quad (4)$$

$$J_3(R) = \int_0^R \xi(r) r^2 dr \quad (5)$$

(Peebles 1980). The quantity $4\pi\bar{n}J_3(R)$ is the mean number of galaxies in excess of random within a distance R of a randomly chosen galaxy (where \bar{n} is the mean galaxy number density). We do not examine the scale dependence of bias in this paper but instead define a single bias factor b from equation (4) with $R = 4 h^{-1}\text{Mpc}$. We compute J_3 in the simulations by simply counting the average number of pairs out to $R = 4 h^{-1}\text{Mpc}$, subtracting the Poisson contribution to obtain the number of excess (correlated) pairs, and dividing by $4\pi\bar{n}$. For a power law correlation function with $\gamma = -2$, the bias factor b is equal to the ratio $r_{0,\text{gal}}/r_{0,\text{dark}}$ of the galaxy and dark matter correlation lengths, and $J_3(R) = r_0^2 R$.

Figure 7 shows the redshift evolution of the bias factor in all of the models. In every case the bias factor drops between $z = 4$ and $z = 2$, and it continues to drop from $z = 2$ to $z = 0$ in the SCDM model. This is the behavior expected from Figure 4, which shows that the galaxy correlation function remains roughly fixed while the dark matter correlation function grows in time, steadily reducing the bias between them. At $z = 3$ the bias factor ranges from $b = 1.3$ in CCDM to $b = 4.2$ in TCDM.

In the one-halo-one-galaxy model, the amplitude of bias is expected to depend on the mass of the parent halos (Mo & White 1996). We might reasonably expect this dependence to carry over into a dependence of bias on galaxy baryon mass. In Figure 8, therefore, we plot the bias factor as a function of baryon mass: $b(M)$ is the bias factor computed from the J_3 integral of all galaxies whose baryon mass exceeds M . We plot b values only if the number of correlated pairs (pairs in excess of the Poisson prediction) exceeds 6.25, so that the shot noise error in the computation of b is less than 25%. The low mass cutoff of the curves corresponds to our mass resolution limit, which is lower in the LCDM and OCDM models because the lower Ω_b implies a lower SPH particle mass. Prior to $z = 2$, the results for the TCDM model are too noisy to allow useful examination of the dependence of bias on galaxy mass.

In most cases, Figure 8 shows a trend of increasing b with increasing galaxy mass. The trend is usually weak at low masses, but in several cases we find considerably stronger bias for the most massive galaxies in the simulation. While mass is likely to be the physical parameter most closely related to b , it is difficult to infer the mass of a Lyman-break galaxy directly from observations. If the star formation rate (and hence the rest frame UV luminosity) is tightly correlated with the galaxy baryon mass, then the Lyman break galaxies that make it into a magnitude limited sample will be the most massive galaxies present at the observed redshift. With this assumption, one can use space density as an observable proxy for galaxy mass. In Figure 9, we plot $b(M)$ as a function of $n(M)$, the comoving space density of galaxies with baryonic mass greater than M . Unfortunately, our box is not large enough to allow statistically reliable measures of b at the space density of the ASGDPK sample. The problem will eventually be rectified with larger volume simulations, and with observational studies that probe clustering further down the luminosity function, but for now the gap between the space densities of the simulated and observed samples is an uncertainty we must live with.

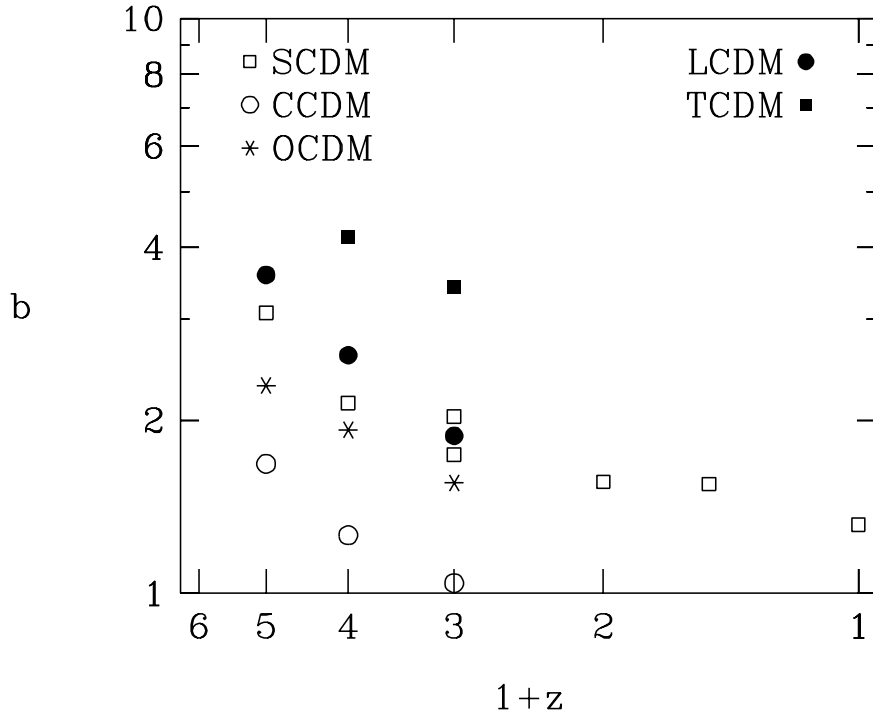


Fig. 7.— Redshift evolution of the bias factor, b . The value of b is computed from eq. (4) using all SPH galaxies. Results for SCDM at $z = 0, 0.5, 1$, and the upper SCDM point at $z = 2$, come from the lower resolution SCDM simulation. The TCDM model is not plotted at $z = 4$ because its correlation function is too noisy.

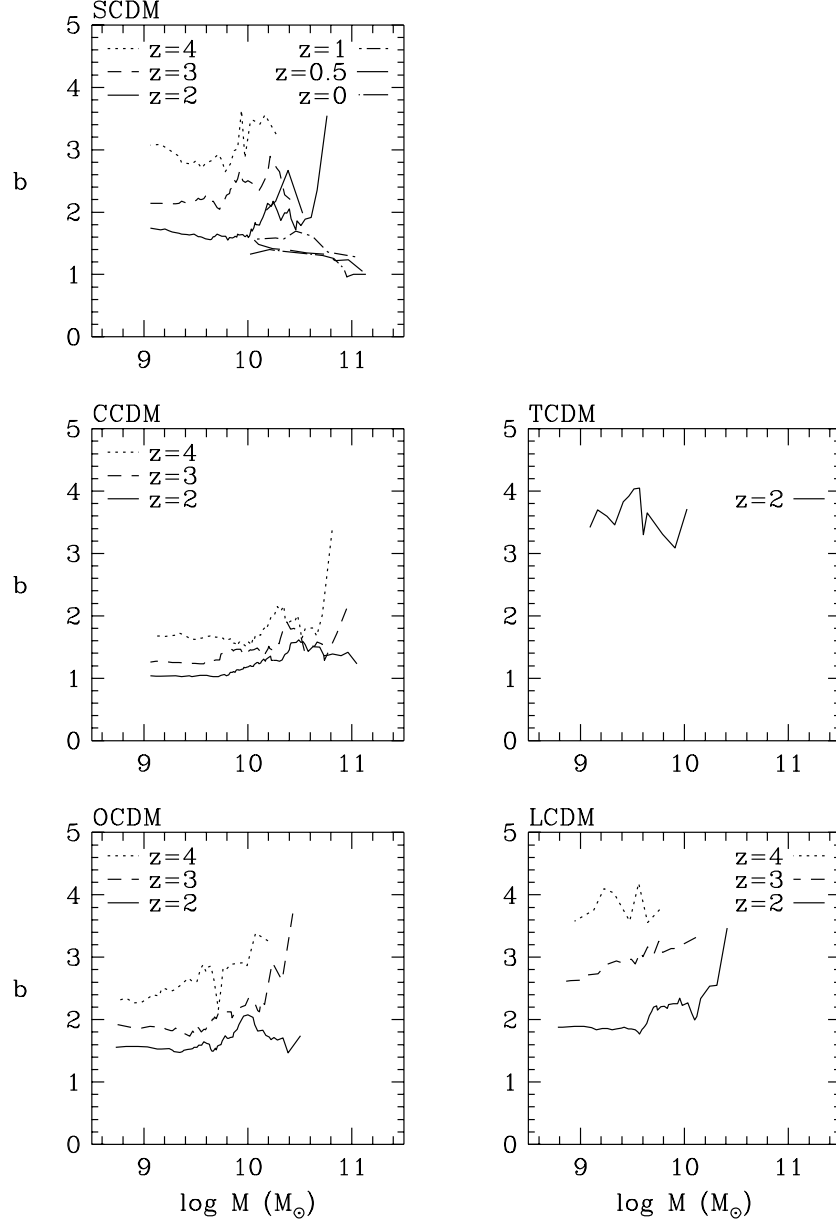


Fig. 8.— Mass dependence of the bias factor. The bias factor $b(M)$ for all galaxies with baryonic mass greater than M is plotted as a function of M , at redshifts $z = 4, 3$, and 2 . Results from the lower resolution SCDM simulation are shown at $z = 2, 1, 0.5$, and 0 .

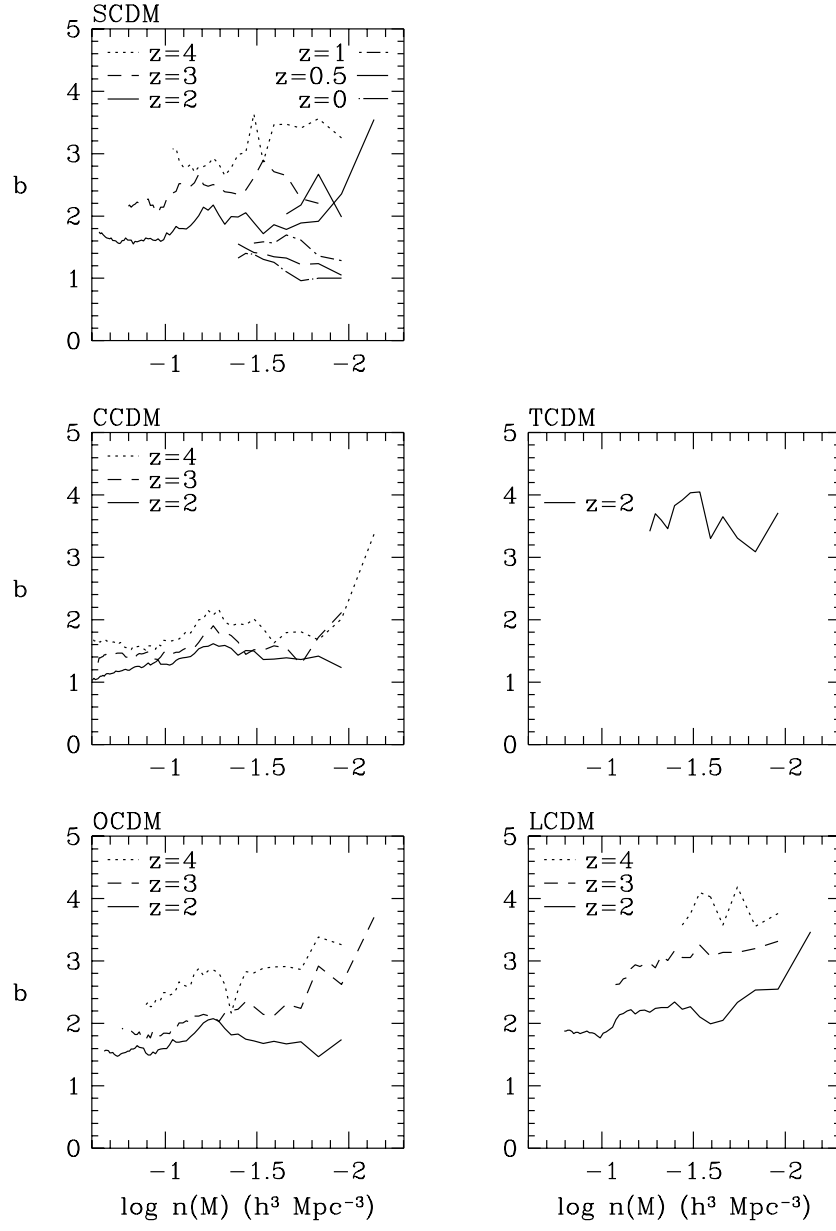


Fig. 9.— Same as Fig. 8, except that $b(M)$ is plotted against $n(M)$, the comoving number density of galaxies with baryonic mass greater than M .

The predicted bias of high redshift galaxies shown in Figures 7–9 is generally (but not always) higher than the estimated bias factor of galaxies today. The determination of b at $z = 0$ is intimately connected to the determination of Ω , and virtually all current analyses measure a combination of b and Ω rather than b alone. For example, the masses of observed galaxy clusters imply that the rms mass fluctuation in $8 h^{-1}\text{Mpc}$ spheres is $\sigma_8 \approx 0.5\Omega^{-0.6}$ (e.g., White, Efstathiou & Frenk 1993; Eke, Cole & Frenk 1996), which in combination with the measured fluctuation amplitude $\sigma_{8,I} = 0.7$ for IRAS-selected galaxies (Fisher et al. 1994) implies a bias factor $b_I \approx 1.4\Omega^{0.6}$. The VELMOD peculiar velocity analysis of Willick & Strauss (1998) and redshift-space distortion analysis of Cole, Fisher, & Weinberg (1995) imply a larger bias factor $b_I \approx 2\Omega^{0.6}$, while the POTENT peculiar velocity analysis of Sigad et al. (1998) implies a lower value, $b_I \approx 1.12\Omega^{0.6}$ (see Strauss & Willick 1995 for a summary of numerous other estimates of b_I). The *relative* bias of optical galaxies to IRAS galaxies can be estimated from direct comparisons of their correlation functions, $b_O/b_I \approx 1.4$ at the $8 h^{-1}\text{Mpc}$ scale (Strauss et al. 1992; Fisher et al. 1994; Moore et al. 1994; Peacock & Dodds 1996), though there are also strong indications that the clustering of optical galaxies depends on luminosity (Hamilton 1988; Park et al. 1994; Loveday et al. 1995). If we accept the mounting but still circumstantial evidence for a low density universe and therefore adopt $\Omega \approx 0.4$, then a reasonable reading of the current constraints would be $b_I \approx 0.7$ and $b_O \approx 1$ at $z = 0$.

3.4. Finite Volume Corrections

As we have already mentioned, the absence of fluctuations on scales larger than the fundamental mode of our $11.111 h^{-1}\text{Mpc}$ simulation cube makes the galaxy correlation length in our simulations artificially low and the correlation function artificially steep. We can estimate the size of this effect by using purely gravitational N-body simulations with larger volume and lower spatial resolution. Specifically, for each cosmological model we perform six simulations using the particle-mesh (PM) code of Park (1990; see also Park & Gott 1991). Each simulation uses 192^3 particles and a 192^3 density-potential mesh to compute the gravitational clustering in a cube $66.66 h^{-1}\text{Mpc}$ on a side, a volume 216 times larger than that of our SPH simulations. The spatial resolution (size of a mesh cell) in the PM simulations is $347(1+z)^{-1}h^{-1}\text{kpc}$ (physical units), compared to the $3(1+z)^{-1}h^{-1}\text{kpc}$ gravitational force softening used in the TreeSPH simulations. We measure the dark matter correlation lengths in the PM simulations using least squares power law fits as before, but we restrict the fit to spatial scales larger than twice the spatial resolution of the PM simulations. We have carried out PM simulations of $11.111 h^{-1}\text{Mpc}$ cubes with the same resolution (i.e., 32^3 particles on a 32^3 mesh) to confirm that the PM simulations reproduce the dark matter correlation function of the TreeSPH simulations on these scales, and to confirm that the mass correlation function obtained for the specific set of initial conditions used in the TreeSPH simulations is similar to the mean mass correlation function obtained in volumes of this size.

We use the results of the larger volume simulations to compute a “finite volume r_0 correction

factor” for each model at each redshift: the ratio of the dark matter correlation length in the large volume simulations to the dark matter correlation length in the corresponding TreeSPH simulation. These correction factors are listed in Table 4; they range from 1.4 to 2.3, with most values in the range 1.9 to 2.2. Thus, our finite simulation volume causes us to underestimate the dark matter correlation length by about a factor of two. The slope of the correlation functions in the larger volume simulations is also shallower, typically $\gamma \approx 1.8$ instead of $\gamma \approx 2.0$.

In order to estimate the *galaxy* correlation lengths that we would obtain in larger volume simulations, we assume that our $11.111 h^{-1}\text{Mpc}$ simulations correctly calculate the *bias* between galaxies and dark matter. While we do not expect this assumption to be precisely correct, since, for example, the abundance of peaks in the initial conditions is modulated by large scale waves (Kaiser 1984; Bardeen et al. 1986), it is likely to be a reasonable first approximation. With this assumption, we simply multiply the galaxy correlation lengths from Table 2 by the correction factors in Table 4 to obtain the corrected galaxy correlation lengths, which are listed in Table 5. At $z \geq 2$, the corrected correlation lengths range from $2.1 h^{-1}\text{Mpc}$ to $3.4 h^{-1}\text{Mpc}$. Figure 10 is a repeat of Figure 6, but it uses the corrected correlation lengths. Since the correction factors are not strongly dependent on redshift, the evolutionary trends are the same as those found previously. The r_0 values listed in Table 5 and plotted in Figure 10 are our best estimates of the predicted correlation lengths for Lyman-break galaxies with $v_c \geq 100 \text{ km s}^{-1}$ ($\Omega = 1$) or $v_c \geq 70 \text{ km s}^{-1}$ ($\Omega = 0.4$). Because the strength of the galaxy clustering is an increasing function of galaxy mass (Figure 8), we expect the correlation lengths of galaxies in existing Lyman-break samples to be somewhat larger, a point that we will return to shortly.

4. Discussion

Our basic results are easy to summarize. While the five CDM models that we examine in this paper differ in their cosmological parameters, differ (substantially) in their mass clustering amplitudes, and differ (slightly) in their initial power spectrum shapes, they predict remarkably similar galaxy clustering at $z = 4, 3$, and 2 . The galaxy correlation functions show almost no evolution over this redshift range, even though the mass correlation functions grow steadily. In most cases the high redshift galaxies are strongly biased tracers of the underlying mass, but the

Table 4: Finite volume r_0 correction factors

Model	$z = 4$	$z = 3$	$z = 2$	$z = 1$	$z = 0$
SCDM	1.59 ± 0.02	1.97 ± 0.01	1.90 ± 0.01	1.98 ± 0.007	2.08 ± 0.004
CCDM	1.87 ± 0.01	1.89 ± 0.01	1.90 ± 0.01	-	-
OCDM	2.06 ± 0.02	2.11 ± 0.01	2.17 ± 0.01	-	-
LCDM	2.09 ± 0.02	2.20 ± 0.02	2.28 ± 0.01	-	-
TCDM	1.38 ± 0.03	1.54 ± 0.03	2.11 ± 0.02	-	-

Table 5: Finite volume corrected correlation lengths, r_0 in $h^{-1}\text{Mpc}$

Model	$z = 4$	$z = 3$	$z = 2$	$z = 1$	$z = 0$
SCDM	2.06 ± 0.05	2.28 ± 0.04	2.27 ± 0.03	3.17 ± 0.18	4.89 ± 0.18
CCDM	2.20 ± 0.03	2.13 ± 0.02	2.34 ± 0.02	-	-
OCDM	2.63 ± 0.05	2.68 ± 0.04	2.77 ± 0.03	-	-
LCDM	3.15 ± 0.15	3.11 ± 0.07	3.07 ± 0.05	-	-
TCDM	2.82 ± 0.47	2.52 ± 0.24	3.36 ± 0.13	-	-

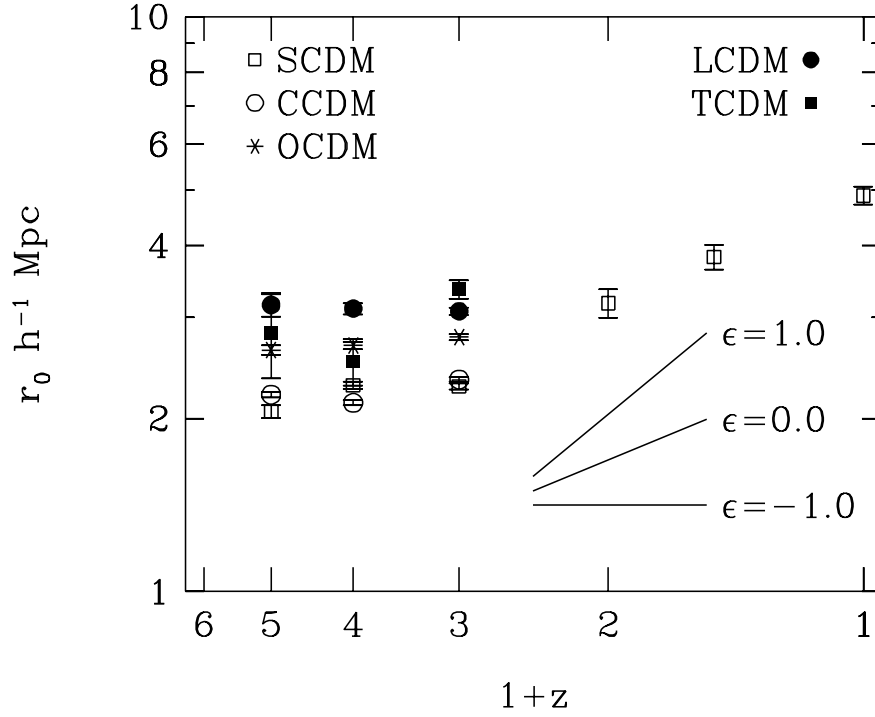


Fig. 10.— Redshift evolution of the galaxy correlation length, as in Fig. 6, with correlation lengths corrected for the effects of the finite simulation volume. Solid lines show the expected growth rates for different values of ϵ (eq. [2]).

bias factor evolves with redshift and varies from model to model, roughly in inverse proportion to the amplitude of mass fluctuations. The more massive galaxies tend to be more highly clustered, though the trend is fairly weak over the mass range for which our $\xi(r)$ measurements are statistically robust. In our lower resolution SCDM simulation evolved to low redshift, the strength of galaxy clustering grows from $z = 2$ to $z = 0$.

The evolution of the galaxy correlation function in our simulations is qualitatively similar to that in analytic models that identify galaxies with high peaks of the initial density field (Bardeen et al. 1986; Bagla 1998b). The galaxies are “born” strongly clustered and highly biased, and at early times the dark matter simply falls into the structures where the galaxies already reside, driving down the bias factor without substantially changing the galaxy correlation function. Eventually the gravitational clustering of the dark matter begins to change the galaxy distribution, and the galaxy $\xi(r)$ increases, as seen at low redshift in the SCDM simulation. The evolution of $\xi(r)$ is similar to that predicted in Fry’s (1996) analytic model, in which an initially biased galaxy distribution follows the dark matter velocity field. Galaxy mergers and ongoing galaxy formation complicate the picture, however, as shown (for example) by the fact that the dark matter clustering actually overtakes the galaxy clustering at $z = 2$ in our CCDM simulation. Tegmark & Peebles (1998) have recently described an elegant generalization of Fry’s (1996) approach that can incorporate ongoing galaxy formation and stochastic bias, but this is presently a framework for calculation rather than a predictive model of clustering evolution. We suspect that the semi-analytic/N-body approach (Governato et al. 1998; Kauffman et al. 1998) would yield similar evolution predictions, but there are no published evolution results to which we can compare at present.

Our prediction of a strongly biased galaxy population at high redshift is similar to the prediction of models that identify Lyman-break galaxies directly with the high mass tail of the dark halo population (Mo & Fukugita 1996; Bagla 1998ab; Coles et al. 1998; Jing & Suto 1998; Wechsler et al. 1998). Like the halo-based calculations, the SPH simulations predict a trend of increasing bias with increasing galaxy mass. The trend appears to be somewhat weaker in the SPH simulations than in the analytic halo model of Mo & White (1996); in particular, we almost always find a positive galaxy bias even with a low circular velocity threshold and a correspondingly high galaxy space density. We also find a positive bias for friends-of-friends halos in an N-body simulation started from the same initial conditions as our SCDM SPH simulation (Figures 2 and 5). The halos show a slightly stronger trend of bias with space density than that of the SPH galaxies, at least for the commonly used linking parameter $d_l = 0.2$ (the halo clustering results also depend on the algorithm and parameters used for halo identification). It is not clear that our findings for halos conflict with previous results, since none that we know of show $\xi(r)$ for low mass, high redshift halos in the non-linear regime, where $\xi(r) \gtrsim 1$. We also note that Jing (1998) finds that in the quasi-linear regime the bias of low mass N-body halos is stronger than the Mo & White (1996) analytic model predicts, though he still finds that the low mass halos are antibiased and finds agreement with the Mo & White (1996) formula for high mass halos. For now, the most

we can say is that the analytic formalism for the bias of halos in the linear regime should be used with some caution, especially if one is interpreting the clustering of galaxies in the non-linear regime, where the Lyman-break galaxy correlation function is presently measured.

Our best estimates of the predicted galaxy correlation lengths are those listed in Table 5 and plotted in Figure 10. At $z = 3$, they lie in the range $2.1 - 3.1 h^{-1}\text{Mpc}$. These predictions apply to the full population of galaxies above our resolution limit. The more massive galaxies are more strongly clustered. One can find the predicted correlation length for galaxies with mass greater than M by multiplying the value in Table 5 by the ratio $[b(M)/b(\text{all})]^{2/|\gamma|} \approx b(M)/b(\text{all})$, read from Figure 8, where $b(\text{all})$ is the bias factor for the full galaxy population (the left end of the $b(M)$ curve). The increase in r_0 is often $30 - 50\%$ or even more for the most massive galaxies, but it is rather uncertain because of our limited statistics.

From an analysis of the angular correlation function of Lyman-break galaxy candidates, Giavalisco et al. (1998a) find $\gamma = -2.0 \pm 0.3$ and a correlation amplitude that corresponds to $r_0 = 2.1 \pm 0.5 h^{-1}\text{Mpc}$ for $\Omega = 1$ or $2.8 \pm 0.7 h^{-1}\text{Mpc}$ for $\Omega = 0.4$ (with either $\Lambda = 0$ or $\Lambda = 0.6$). ASGDPK estimate a significantly higher correlation length, $r_0 = 4 \pm 1 h^{-1}\text{Mpc}$ ($\Omega = 1$), $r_0 = 5 \pm 1 h^{-1}\text{Mpc}$ ($\Omega = 0.2$, $\Lambda = 0$), or $r_0 = 6 \pm 1 h^{-1}\text{Mpc}$ ($\Omega = 0.3$, $\Lambda = 0.7$), from a counts-in-cells analysis of spectroscopically confirmed Lyman-break objects.¹ The effective redshift of both determinations is $z \approx 3$, and the difference between them provides an indication of the current level of measurement uncertainties.

Quantitative comparison between our results and these data is hampered by the non-overlapping space densities of the theoretical and observational samples. However, it at least seems clear that the models considered in this paper have no difficulty explaining the strong observed clustering of Lyman-break galaxies. Indeed, with a reasonable extrapolation of the $b(M)$ vs. $n(M)$ curves in Figure 9, it seems that some of the models might overpredict even the stronger clustering found by ASGDPK. Interpreting their results in light of the Mo & White (1996) halo biasing formula, ASGDPK conclude that their data favor a $\Gamma = 0.2$ shape parameter for the primordial mass power spectrum over $\Gamma = 0.5$, but we find that the predicted galaxy correlation function in the SPH simulations (admittedly at a space density higher than that of the ASGDPK sample) depends only weakly on the shape or amplitude of the underlying mass power spectrum.

Steidel et al. (1998b) report preliminary results (from Giavalisco et al. 1998b) for the clustering of lower luminosity Lyman-break galaxies, derived from the angular correlation function of U -band dropouts in the Hubble Deep Field (HDF; Williams et al. 1996). The estimated space density of this sample is 45 times higher than that of the ASGDPK sample, and the estimated bias factor is 3 times lower (Steidel et al. 1998b, figure 7). Since the correlation length scales as $r_0 \propto b^{2/|\gamma|}$, this

¹ Scaling the $\Omega = 1$ results by the ratios of angle-distance or redshift-distance relations yields $r_0 \approx 5.5 \pm 1.4 h^{-1}\text{Mpc}$ for the parameters of our OCDM and LCDM models; the scaling in ASGDPK is somewhat different because they estimate r_0 separately for each cosmology using cubical cells whose redshift depth matches the angular size of the survey field.

lower bias factor implies (in combination with the ASGDPK results) $r_0 \sim 1.2 \ h^{-1}\text{Mpc}$ for $\Omega = 1$ and $r_0 \sim 1.6 \ h^{-1}\text{Mpc}$ for $\Omega = 0.4$, assuming $\gamma = -1.8$. At the space density of the HDF sample there would be ~ 120 galaxies in our $\Omega = 1$ simulation boxes and ~ 50 galaxies in our $\Omega = 0.4$ simulation boxes, so it is reasonable to compare these numbers directly to the correlation lengths in Table 5. The simulations appear to predict excessively strong clustering for the Giavalisco et al. (1998b) HDF sample, particularly with $\Omega = 1$.

Given the current observational and theoretical uncertainties, it is premature to make much of this conflict, which at present has only marginal statistical significance. One source of theoretical uncertainty, the small size of our simulation volumes, is purely technical, and it will be remedied in the near future with larger simulations. The other source of theoretical uncertainty, the unknown relation between galaxy baryon mass and rest-frame UV luminosity, is more fundamental. Because the clustering strength depends on galaxy mass (Figure 8), the correlation function predicted for a given Lyman-break sample depends on how that sample probes the galaxy mass function. Our conversion from galaxy mass to space density in Figure 9 implicitly assumes that the mass-luminosity relation is monotonic, so that a magnitude limited sample selects galaxies at the top end of the mass function. If episodic star formation or stochastic dust extinction introduce large scatter into the relation between galaxy mass and UV luminosity, then the predicted relation between clustering strength and space density will be flatter and the predicted clustering for bright Lyman-break galaxy samples will be lower.

Some papers on high redshift structure (e.g., Coles et al. 1998; Jing & Suto 1998) conclude that measurements of Lyman-break galaxy clustering will in time provide valuable tests of cosmological models. Other authors have argued that these measurements will ultimately teach us more about the nature of Lyman-break galaxies themselves (e.g., SADGPK; Giavalisco et al. 1998a; ASGDPK). In this debate, we side firmly with the latter group. We have examined models with very different mass clustering properties, but the effects of biased galaxy formation conspire to erase the differences between them. This “conspiracy” is not as suspicious as it initially seems; it simply reflects the fact that galaxies form at similar “special” locations in the density fields of the different models and therefore have similar spatial correlations (Figure 1). The Ly α forest provides a more straightforward route to testing the high redshift structure predictions of cosmological theories because the physics of the absorbing medium is relatively simple and leads to a direct relation between an observable quantity, the Ly α optical depth, and the underlying mass density (WKH). Indeed, the determination of the high redshift mass power spectrum by the method of Croft et al. (1998) will yield the bias factor of Lyman-break galaxies as a by-product.

Given the complications introduced by bias, we think it is better to regard Lyman-break galaxy clustering as a probe of galaxy formation physics rather than a test of cosmological models. The fact that the SPH simulations (and other approaches based on peaks, halos, or semi-analytic models) account naturally for the observed strong clustering is already an encouraging success for the general scenario of hierarchical galaxy formation from Gaussian primordial density fluctuations. Comparison between the predicted trend of clustering strength against galaxy mass

and the observable trend of clustering strength against luminosity can provide a more detailed test of theoretical models and an indication of whether the instantaneous star formation rate is tightly correlated with galaxy mass. This line of argument has already been pursued by SADGPK and ASGDPK in the context of halo models. In the context of SPH simulations, the trend of clustering with UV luminosity can ultimately help to test whether our adopted paradigm for galactic scale star formation is basically correct or whether galaxy interactions or stochastic bursts have a strong influence on a high redshift galaxy’s star formation rate. The study of high redshift galaxy clustering is still in its early phases, but progress in both observation and theory has been remarkably rapid, and it looks likely to continue.

We thank Eric Linder, Max Pettini, and Chuck Steidel for useful discussions and Houjun Mo and Yipeng Jing for helpful exchanges about halo clustering. We thank Changbom Park for allowing us to use his PM N-body code. This work was supported by NASA Astrophysical Theory Grants NAG5-3922, NAG5-3820, and NAG5-3111, by NASA Long-Term Space Astrophysics Grant NAG5-3525, and by the NSF under grants ASC93-18185 and ACI96-19019. The simulations were performed at the San Diego Supercomputer Center.

REFERENCES

- Adelberger, K. L., Steidel, C. C., Giavalisco, M., Dickinson, M., Pettini, M., & Kellogg, M. 1998, ApJ, in press, astro-ph/9804236 (ASGDPK)
- Bagla, J.S. 1998a, MNRAS, submitted, astro-ph/9707159
- Bagla, J.S. 1998b, MNRAS, submitted, astro-ph/9711081
- Bardeen, J., Bond, J.R., Kaiser, N. & Szalay, A.S. 1986, ApJ, 304, 15
- Barnes, J.E. & Hut, P. 1986, Nature, 324, 446
- Baugh, C. M., Cole, S., Frenk, C. S., & Lacey, C. G. 1998, ApJ, 498, 504
- Bennett, C., L., Banday, A. J., Górski, K. M., Hinshaw, G., Jackson, P., Keegstra, P., Kogut, A., Smoot, G. F., Wilkinson, D. T. & Wright, E. L. 1996, ApJ, 646, L1
- Blumenthal, G. R., Faber, S. M., Primack, J. R., & Rees, M. J. 1984, Nature, 311, 517
- Burles, S., & Tytler, D. 1997, AJ, 114, 1330
- Burles, S., & Tytler, D. 1998, ApJ, in press, astro-ph/9712108
- Cole, S., Aragon-Salamanca, A., Frenk, C. S., Navarro, J. F., & Zepf, S. E. 1994, MNRAS, 271, 781
- Cole, S., Fisher, K. & Weinberg, D. H. 1995, MNRAS, 275, 515
- Cole, S., Weinberg, D. H., Frenk, C. S., & Ratra, B. 1997, MNRAS, 289, 37
- Coles, P., Lucchin, F., Matarrese, S., & Moscardini, L. 1998, MNRAS, submitted, astro-ph/9803197
- Croft, R.A.C., Weinberg, D.H., Katz, N. & Hernquist, L. 1998, ApJ, 495, 44
- Efstathiou, G., Bernstein, G., Katz, N., Tyson, J.A. & Guhathakurta, P. 1991, ApJ, 380, L47
- Eke, V. R., Cole, S. & Frenk, C. S. 1996, MNRAS, 282, 263
- Fisher, K.B., Davis, M., Strauss, M.A., Yahil, A. & Huchra, J.P. 1994, MNRAS, 266, 50
- Frenk, C. S., White, S. D. M., Davis, M., & Efstathiou, G. 1988, ApJ, 327, 507
- Fry, J.N. 1996, ApJ, 461, L65
- Gardner, J.P., Katz, N., Hernquist & Weinberg, D.H. 1997, ApJ, 484, 31
- Gelb, J. M. & Bertschinger, E. 1994a, ApJ, 436, 467
- Gelb, J. M. & Bertschinger, E. 1994b, ApJ, 436, 491

- Giavalisco, M., Steidel, C.C., Adelberger, K.L., Dickinson, M.E., Pettini, M. & Kellogg, M. 1998a, ApJ, in press, astro-ph/9802318
- Giavalisco et al. 1998b, in preparation
- Gingold, R.A. & Monaghan, J.J. 1977, MNRAS, 181, 375
- Groth, E.J. & Peebles, P.J.E. 1977, ApJ, 217, 385
- Governato, F., Baugh, C.M., Frenk, C.S., Cole, S., Lacey, C.G., Quinn, T.R. & Stadel, J. 1998, Nature, 392, 359
- Haardt, F. & Madau, P. 1996, ApJ, 461, 20
- Hamilton, A. J. S. 1988, ApJ, 331, L59
- Hernquist, L. 1987, ApJS, 64, 715
- Hernquist, L. & Katz, N. 1989, ApJS, 70, 419
- Jing, Y.P. 1998, ApJ, submitted, astro-ph/9805202
- Jing, Y.P. & Suto, Y. 1998, ApJ, 494, L5
- Kaiser, N. 1984, ApJ, 294, L9
- Katz, N., Hernquist, L. & Weinberg, D.H. 1992, ApJ, 399, L109
- Katz, N., Weinberg D.H. & Hernquist, L. 1996, ApJS, 105, 19 (KWH)
- Kauffmann, G., Colberg, J. M., Diaferio, A., & White, S. D. M. 1998, MNRAS, submitted, astro-ph/9805283
- Loveday, J., Maddox, S. J., Efstathiou, G., & Peterson, B. A. 1995, ApJ, 442, 457
- Lowenthal, J.D., Koo, D.C., Guzmán, R., Gallego, J., Phillips, A.C., Faber, S.M., Vogt, N.P., Illingworth, G.D. & Gronwall, C. 1997, ApJ, 481, 673
- Lucy, L. 1977, AJ, 82, 1013
- Miralles, J.M. & Pelló, R. 1998, astro-ph/9801062
- Mo, H.J. & Fukugita, M. 1996, ApJ, 467, L9
- Mo, H.J. & White S.D.M. 1996, MNRAS, 282, 1096
- Moore, B., Frenk, C. S., Efstathiou, G. & Saunders, W. 1994, MNRAS, 269, 742
- Moscardini, L., Coles, P., Lucchin, F. & Matarrese, S. 1998, astro-ph/9712184

- Owen, J. M., Weinberg, D. H., & Villumsen, J. V. 1998, ApJ, submitted, astro-ph/9805097
- Park, C. 1990, PhD Thesis, Princeton University
- Park, C., & Gott, J. R. 1991, MNRAS, 249, 288
- Park, C., Vogeley, M. S., Geller, M. J., & Huchra, J. P. 1994, ApJ, 431, 569
- Peacock, J. A. & Dodds, S. J. 1996, MNRAS, 280, L19
- Pearce, F. R. 1998, A&A, submitted, astro-ph/9803133
- Peebles, P. J. E. 1980, The Large Scale Structure of the Universe (Princeton: Princeton University Press)
- Peebles, P. J. E. 1982, ApJ, 263, L1
- Quashnock, J. M., Vanden Berk, D. E. & York, D. G. 1996, ApJ, 472, L69
- Quashnock, J. M. & Vanden Berk, D. E. 1997, ApJ, submitted, astro-ph/9706233
- Quinn, T., Katz, N., Stadel, J. & Lake, G. 1998, ApJ, in preparation
- Ratra, B., Sugiyama, N., Banday, A. J. & Górski, K. M. 1997, ApJ, 481, 22
- Rauch, M., Miralda-Escudé, J., Sargent, W.L.M., Barlow, T.A., Weinberg, D.H., Hernquist, L., Katz, N., Cen, R. & Ostriker, J.P. 1997, ApJ, 489, 7
- Sigad, Y., Eldar, A., Dekel, A., Strauss, M.A. & Yahil, A., ApJ, 495, in press, astro-ph/9708141
- Steidel, C.C, Giavalisco, M., Pettini, M., Dickinson, M.E. & Adelberger, K.L. 1996, ApJ, 462, L17
- Steidel, C.C, Adelberger, K.L., Dickinson, M.E, Giavalisco, M., Pettini, M. & Kellogg, M. 1998a ApJ, 492, 428 (SADGPK)
- Steidel, C.C, Adelberger, K.L., Dickinson, M.E, Giavalisco, M., Pettini, M. & Kellogg, M. 1998b, Phil Trans Roy Soc London, submitted, astro-ph/9805267
- Strauss, M. A., Davis, M., Yahil, A. & Huchra, J. P. 1992, ApJ, 385, 421
- Strauss, M.A. & Willick, J.A., 1995, Physics Reports, 261, 271
- Tegmark, M., & Peebles, P. J. E. 1998, ApJ, submitted, astro-ph/9804067
- Villumsen, J.V., Freudling, W. & da Costa, L.N. 1997, ApJ, 481, 578
- Walker, T.P., Steigman, G., Schramm, D.N., Olive, K.A. & Kang, H.S, 1991, ApJ, 376, 51
- Wechsler, R.H., Gross, M.K., Primack, J.R., Blumenthal, G.R. & Dekel, A. 1998, ApJ, submitted, astro-ph/9712141

- Weinberg, D.H., Hernquist, L. & Katz, N. 1997, ApJ, 477, 8 (WHK)
- Weinberg, D. H., Katz, N., & Hernquist, L. 1998, in *Origins*, eds. J. M. Shull, C. E. Woodward, & H. Thronson, (ASP Conference Series: San Francisco), astro-ph/9708213, (WKH)
- White, S. D. M., Efstathiou, G. P. & Frenk, C. S. 1993, MNRAS, 262, 1023
- Williams, R. E., et al. 1996, AJ, 112, 1335
- Willick, J. A. & Strauss, M. A. 1998, ApJ, submitted, astro-ph/9801307